

# Charge-Carrier Dynamics of Solution-Processed Antimony- and Bismuth-Based Chalcogenide Thin Films

Zhenglin Jia,<sup>#</sup> Marcello Righetto,<sup>#</sup> Yujie Yang, Chelsea Q. Xia, Yanyan Li, Ruiming Li, Yuwei Li, Bin Yu, Yong Liu, Huiming Huang, Michael B. Johnston, Laura M. Herz,<sup>\*</sup> and Qianqian Lin<sup>\*</sup>



Cite This: *ACS Energy Lett.* 2023, 8, 1485–1492



Read Online

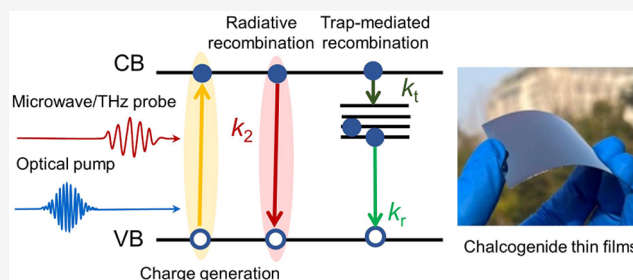
ACCESS |

Metrics & More

Article Recommendations

Supporting Information

**ABSTRACT:** Chalcogenide-based semiconductors have recently emerged as promising candidates for optoelectronic devices, benefiting from their low-cost, solution processability, excellent stability and tunable optoelectronic properties. However, the understanding of their fundamental optoelectronic properties is far behind the success of device performance and starts to limit their further development. To fill this gap, we conduct a comparative study of chalcogenide absorbers across a wide material space, in order to assess their suitability for different types of applications. We utilize optical-pump terahertz-probe spectroscopy and time-resolved microwave conductivity techniques to fully analyze their charge-carrier dynamics. We show that antimony-based chalcogenide thin films exhibit relatively low charge-carrier mobilities and short lifetimes, compared with bismuth-based chalcogenides. In particular, AgBiS<sub>2</sub> thin films possess the highest mobility, and Sb<sub>2</sub>S<sub>3</sub> thin films have less energetic disorder, which are beneficial for photovoltaic devices. On the contrary, Bi<sub>2</sub>S<sub>3</sub> showed ultralong carrier lifetime and high photoconductive gain, which is beneficial for designing photoconductors.



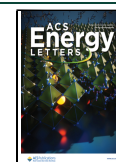
Antimony- and bismuth-based chalcogenide semiconductors have attracted tremendous attention in the field of optoelectronics, benefiting from the facile and low-cost processing, superior stability, and ultrahigh and tunable absorption coefficients. In recent years, they have demonstrated great potential for multiple applications, ranging from next-generation thin-film photovoltaics,<sup>1–4</sup> photodetectors,<sup>5,6</sup> and phototransistors,<sup>7,8</sup> to photocatalysis.<sup>9,10</sup> In particular, solution-processed Sb<sub>2</sub>S<sub>3</sub> and AgBiS<sub>2</sub>-based solar cells have progressed rapidly. For example, Tang et al. proposed a vacuum-assisted solution process for highly efficient Sb<sub>2</sub>S<sub>3</sub> solar cells and achieved a power conversion efficiency (PCE) of 6.78%.<sup>11</sup> Wang and coauthors deposited Sb<sub>2</sub>S<sub>3</sub> thin films via chemical bath deposition with multiple sulfur sources, and realized a new PCE record of >8%.<sup>12</sup> To extend the absorption range, selenium was also introduced in antimony-based chalcogenides. Recently, Tang and co-workers fabricated efficient Sb<sub>2</sub>(S,Se)<sub>3</sub> solar cells via the hydrothermal method, and pushed the PCE over 10%.<sup>13</sup> Furthermore, Bernechea et al. also reported a relatively high PCE of 6.3% based on AgBiS<sub>2</sub> nanocrystals,<sup>14</sup> and Wang et al. further updated the efficiency to 9.17% based on cation disorder engineering.<sup>15</sup> Kim and coauthors also reported solar cells with

>9% PCE based on AgBiS<sub>2</sub>/organic hybrids.<sup>16</sup> Additionally, AgSbS<sub>2</sub> and Bi<sub>2</sub>S<sub>3</sub> were also proposed as promising semiconductors for photovoltaics. However, the power conversion efficiencies of AgSbS<sub>2</sub>- and Bi<sub>2</sub>S<sub>3</sub>-based solar cells are still lagging behind.<sup>17,18</sup> On the other hand, chalcogenides have also emerged as promising candidates for photodetection. Jiang and co-workers reported highly efficient and ultrafast photodiodes based on AgBiS<sub>2</sub> precursors.<sup>19</sup> Zhao et al. reported direct polarimetric image sensors based on Sb<sub>2</sub>S<sub>3</sub> nanowires with a wide spectral response.<sup>20</sup> Xu et al. developed narrowband photodiodes based on a set of chalcogenide thin films with various bandgaps.<sup>21</sup> Huang and coauthors introduced Sb<sub>2</sub>S<sub>3</sub> thin films for photodetection with a field-effect transistor structure.<sup>22</sup> Jiang et al. and Yang et al. also

Received: January 18, 2023

Accepted: February 14, 2023

Published: February 17, 2023



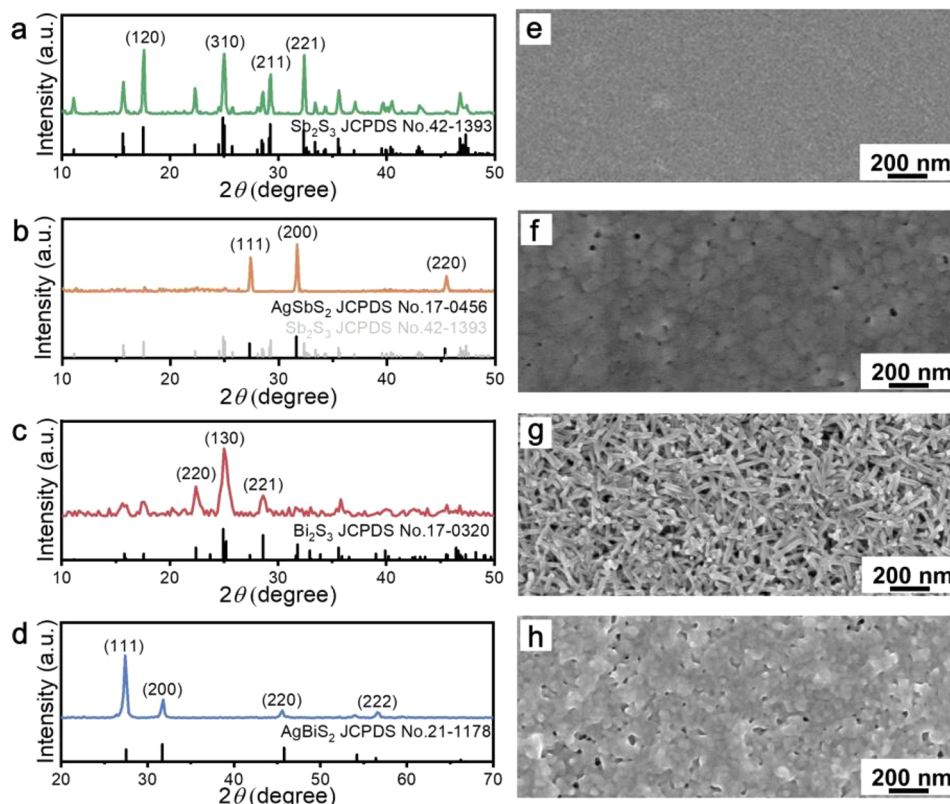


**Figure 1.** XRD patterns of the solution-processed (a)  $\text{Sb}_2\text{S}_3$ , (b)  $\text{AgSbS}_2$ , (c)  $\text{Bi}_2\text{S}_3$ , and (d)  $\text{AgBiS}_2$  thin films. SEM images of the (e)  $\text{Sb}_2\text{S}_3$ , (f)  $\text{AgSbS}_2$ , (g)  $\text{Bi}_2\text{S}_3$ , and (h)  $\text{AgBiS}_2$  samples.

reported phototransistors based on  $\text{AgBiS}_2$  and  $\text{AgSbS}_2$ , respectively, and achieved a tunable photogating effect.<sup>7,23</sup>

Despite these recent achievements, the device-centric development of chalcogenide semiconductors observed in the past years has been based mostly on trial–error approaches in device and materials engineering. Therefore, new crucial insights into charge-carrier generation, recombination and transport processes are urgently needed to reveal structure–function relations and provide essential feedback for device optimization. A more general understanding of the physics behind charge-carrier dynamics and transport in these materials is an indispensable prerequisite for revealing fundamental limits and prospects of these chalcogenide thin films for a wide range of optoelectronic applications. To fill this gap, we use optical-pump-terahertz-probe (OPTP) spectroscopy and time-resolved microwave conductivity (TRMC) to investigate the optoelectronic properties of solution-processed chalcogenide thin films across a wide range of compositions, i.e.,  $\text{Sb}_2\text{S}_3$ ,  $\text{AgSbS}_2$ ,  $\text{Bi}_2\text{S}_3$  and  $\text{AgBiS}_2$ . Different from conventional ultrafast optical probes (e.g., time-resolved photoluminescence and transient absorption), OPTP and TRMC probe the ultrafast and fast time-resolved photoconductivity, thus giving direct access to device-relevant parameters such as charge-carrier mobility and diffusion lengths and allowing an assessment of these materials in terms of their suitability across a wide device application space. Furthermore, we complement these measurements with temperature-dependent conductivity experiments to investigate the intrinsic charge-carrier densities and photoconductivity gain. We then combine the resulting parameters (i.e., charge-carrier mobility, recombination constants) with a complete structural characterization of the thin films to derive general structure–property relations. These

results reveal the complex interplay of factors behind the performance of chalcogenide-based optoelectronic devices, thereby providing essential feedback to advance the frontiers of chalcogenide thin-film fabrication.

In this work, we focus on the recently developed solution-processed antimony- and bismuth-based chalcogenide thin films, i.e.,  $\text{Sb}_2\text{S}_3$ ,  $\text{AgSbS}_2$ ,  $\text{Bi}_2\text{S}_3$  and  $\text{AgBiS}_2$ . We fabricated thin films of these materials by spin-coating from precursor solutions in polar organic solvents, as described in the Methods section (see [Supporting Information](#)). X-ray diffraction (XRD) patterns of these films further confirmed the formation of corresponding crystal phases, as shown in [Figure 1d](#), which are consistent with the characteristic peaks of the standard Joint Committee on Powder Diffraction Standards (JCPDS) cards. It is also worth to note that the  $\text{AgSbS}_2$  samples showed very weak impurity peaks, which could be identified as the characteristic peaks of  $\text{Sb}_2\text{S}_3$ . We also inferred the crystallite size ( $D$ ) of these chalcogenide films based on the Scherrer equation,<sup>24</sup> given by

$$D = \frac{k\lambda}{B\cos\theta} \quad (1)$$

where  $\lambda$  is the wavelength of the incident X-ray.  $B$  is the full width half-maximum (FWHM) of the diffraction peak.  $\theta$  is the diffraction angle and  $k$  is shape factor. Then,  $\text{Sb}_2\text{S}_3$ , the crystal crystallite sizes of  $\text{AgSbS}_2$ ,  $\text{Bi}_2\text{S}_3$  and  $\text{AgBiS}_2$  were determined to be 40 nm, 24, 18, and 27 nm, respectively, and all the fabricated films exhibited smooth and reflective surfaces, as shown in [Figure S1](#). [Figure S2](#) also depicts the uniform morphology and surface roughness recorded with an optical microscope and a profilometer. In addition, these solution-processed chalcogenide thin films can also be deposited on

large area (5 cm × 5 cm) flexible substrates as shown in Figure S3.

It is worth noting that the average crystallite size determined by the Scherrer equation could be not necessary the same as the grain size observed from surface morphology.<sup>25</sup> Hence, we also characterized the surface morphology at the nanoscale by using scanning electron microscopy (SEM), as shown in Figure 1e–h. Interestingly, we found that the films possess distinct crystal grains and morphology. The Sb<sub>2</sub>S<sub>3</sub> thin films showed the smallest grain size with negligible pin-holes. On the contrary, AgSbS<sub>2</sub> exhibited relatively large crystal grains but noticeable pin-holes. More interestingly, the Bi<sub>2</sub>S<sub>3</sub> thin films are composed of nanorods with sharp crystal boundaries (Figure 1f and Figure S4), indicating the formation of relatively large Bi<sub>2</sub>S<sub>3</sub> crystal grains. The one-dimensional nanorod morphology is also consistent with literature reports, in which is mainly attributed to the prevalence of strong covalent Bi–S bonds along the [010] direction, whereas only weak van der Waals bonds are present along the [100] and [001] directions between the [Bi<sub>4</sub>S<sub>6</sub>]<sub>n</sub> ribbons.<sup>26</sup> On the other hand, AgBiS<sub>2</sub> films exhibited increased crystal size with more compact and dense morphology, after Ag(I) is introduced in the Bi<sub>2</sub>S<sub>3</sub> precursor. Compared with the AgSbS<sub>2</sub> thin films, AgBiS<sub>2</sub> samples also presented more obvious grain boundaries, suggesting lower content of amorphous regions.

Having knowledge of the crystallinity and morphology of these solution-processed chalcogenide thin films, we now turn to characterizing their optoelectronic properties. Figure S5 displays the transmittance and reflectance spectra of these four thin-film samples measured with an integrating sphere from ultraviolet to near-infrared. We combined the transmittance and reflectance spectra to extract the absorption spectra (Figure S6). By normalizing the film thickness, we can further obtain their absorption coefficient, as shown in Figure 2a, which is crucial for properly designing devices. Sb<sub>2</sub>S<sub>3</sub> thin films showed the widest bandgap ( $E_g$ ) of ~1.73 eV with a sharp Urbach tail (~70 meV). The introduction of Ag(I) in Sb<sub>2</sub>S<sub>3</sub> precursors yielded a decreased  $E_g$  (1.51 eV) and a larger Urbach Energy ( $E_u$ ) of 147 meV. It is worth noting that the bandgap and Urbach tails may vary slightly owing to the film processing and could also be dependent on the composition.<sup>7</sup> Overall, the comparison between antimony- and bismuth-based chalcogenides reveals that the latter present enhanced absorption coefficients ( $\alpha$ ) and reduced bandgaps. The Bi<sub>2</sub>S<sub>3</sub> thin films possess a bandgap of 1.46 eV and  $E_u$  of 113 meV, and the AgBiS<sub>2</sub> films have the smallest bandgap of 1.15 eV with a  $E_u$  of 116 meV. In particular, the AgBiS<sub>2</sub> films exhibited an extremely high  $\alpha$  of  $>10^5$  cm<sup>-1</sup> over the whole visible region, thus confirming the possibility of achieving efficient ultrathin (~35 nm) AgBiS<sub>2</sub>-based solar cells.<sup>15</sup> In addition, we also performed temperature-dependent photoluminescence (PL) spectra of these chalcogenide thin films as shown in Figure S7. All the chalcogenide thin films exhibited extremely weak emission at room temperature, and the PL spectra were relatively broad. With the decrease of temperature, PL intensity increased significantly and the FWHM of the PL spectra also reduced. We then extracted the activation energy ( $E_a$ ) of these chalcogenide thin films based on the Arrhenius equation<sup>27</sup>

$$I(T) = \frac{I_0}{1 + A e^{-E_a/k_B T}} \quad (2)$$

where  $I_0$  is the intensity at 0 K, and  $k_B$  is the Boltzmann constant. All the samples resulted relatively low  $E_a$  values of

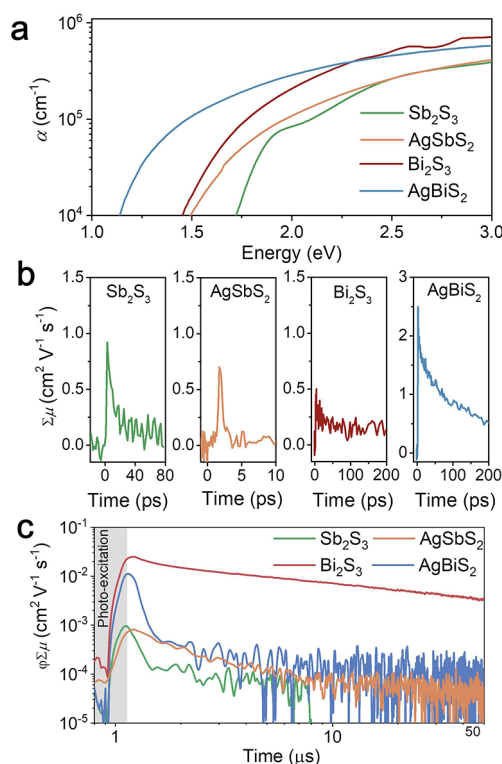


**Figure 2.** Comparison of the (a) absorption coefficient, (b) OPTP, and (c) TRMC decays of Sb<sub>2</sub>S<sub>3</sub>, AgSbS<sub>2</sub>, Bi<sub>2</sub>S<sub>3</sub>, and AgBiS<sub>2</sub> thin films. The OPTP measurements were excited with a 400 nm femtosecond laser with a fluence of ~70 μJ cm<sup>-2</sup>, and the TRMC tests were excited with a 532 nm nanosecond laser with a fluence of ~20 μJ cm<sup>-2</sup>.

30.8 ± 4.4 ~ 37.4 ± 5.0 meV, which is close to the thermal energy at room temperature (26 meV), reflecting the nonexcitonic feature. Therefore, the optoelectronic devices based on these chalcogenide thin films with planar structure can also work efficiently.<sup>15</sup> It is also interesting to note that the Bi<sub>2</sub>S<sub>3</sub> thin films with nanorod structure showed relatively narrower PL spectra, compared with other samples. Considering the relatively narrower bandgap and dispersive absorption tail, Bi<sub>2</sub>S<sub>3</sub> should in principle present a less excitonic feature. Hence, the slightly enhanced PL could be attributed to the quantum confinement effect.

Furthermore, we also evaluated the charge-carrier dynamics of these materials following visible photoexcitation by using OPTP and TRMC spectroscopies, as shown in Figure 2b,c. We observe from OPTP measurements that antimony-based chalcogenide thin films show relatively large initial mobilities (Table 1), ~0.9 and 0.7 cm<sup>2</sup> V<sup>-1</sup> s<sup>-1</sup> for Sb<sub>2</sub>S<sub>3</sub> and AgSbS<sub>2</sub>, respectively. However, the photoconductivity signal was observed to decay in the first few tenths of picoseconds. This behavior is consistent with the ultrafast trapping and self-trapping already reported for Sb<sub>2</sub>S<sub>3</sub> and can be ascribed to several factors, such as the strong coupling with phonons, extensive surface defects, and the quasi-1D structure of these materials.<sup>28,29</sup> On the other hand, bismuth sulfide exhibited relatively lower OPTP mobility of 0.5 ± 0.2 cm<sup>2</sup> V<sup>-1</sup> s<sup>-1</sup>, but the longest charge-carrier lifetime based on the observed OPTP decay. More surprisingly, AgBiS<sub>2</sub> showed the highest OPTP mobility of >2.5 cm<sup>2</sup> V<sup>-1</sup> s<sup>-1</sup> and a considerably longer lifetime. Here, we note that the strongest photoconductivity signal observed from the AgBiS<sub>2</sub> samples is a promising



Table 1. Comparison of the Optoelectronic Properties of Solution-Processed Sb<sub>2</sub>S<sub>3</sub>, AgSbS<sub>2</sub>, Bi<sub>2</sub>S<sub>3</sub>, and AgBiS<sub>2</sub> Thin Films

	Bandgap (E <sub>g</sub> ) [eV]	Urbach Energy (E <sub>u</sub> ) [meV]	OPTP Mobility (μ <sub>OPTP</sub> ) [cm <sup>2</sup> V <sup>-1</sup> s <sup>-1</sup> ]	TRMC Mobility-yield product (φμ <sub>TRMC</sub> ) [cm <sup>2</sup> V <sup>-1</sup> s <sup>-1</sup> ]	Conductivity (σ) extracted from dark J–V @ RT [S cm <sup>-1</sup> ]	Carrier density (n) determined from σ and φμ <sub>TRMC</sub> [cm <sup>-3</sup> ]
Sb <sub>2</sub> S <sub>3</sub>	1.73	70	0.9 ± 0.1	0.003 ± 0.001	5.2 × 10 <sup>-9</sup>	1.1 × 10 <sup>13</sup>
AgSbS <sub>2</sub>	1.51	147	0.7 ± 0.3	0.002 ± 0.001	7.2 × 10 <sup>-7</sup>	2.3 × 10 <sup>15</sup>
Bi <sub>2</sub> S <sub>3</sub>	1.46	113	0.5 ± 0.2	0.032 ± 0.002	7.1 × 10 <sup>-6</sup>	1.4 × 10 <sup>15</sup>
AgBiS <sub>2</sub>	1.15	116	2.5 ± 0.2	0.013 ± 0.001	9.4 × 10 <sup>-6</sup>	4.5 × 10 <sup>15</sup>

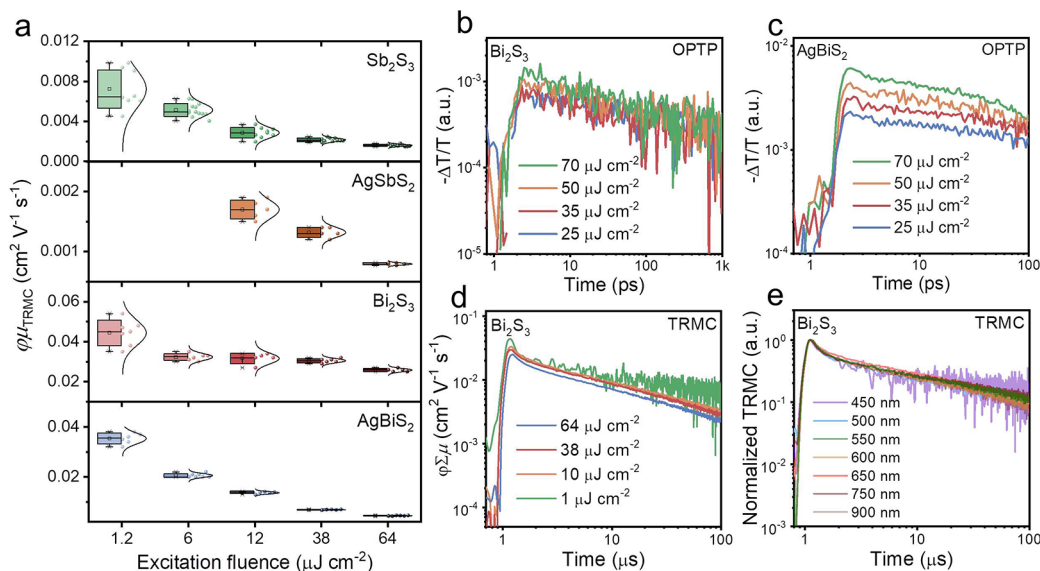


Figure 3. (a) Fluence dependent TRMC mobility-yield products of Sb<sub>2</sub>S<sub>3</sub>, AgSbS<sub>2</sub>, Bi<sub>2</sub>S<sub>3</sub>, and AgBiS<sub>2</sub>. Comparison of the fluence dependent OPTP decays of (b) Bi<sub>2</sub>S<sub>3</sub> and (c) AgBiS<sub>2</sub> thin films, and the comparison of the (d) fluence dependent and (e) wavelength dependent TRMC decays of Bi<sub>2</sub>S<sub>3</sub> thin films.

indication of improved optoelectronic properties. Furthermore, we also probed the materials with TRMC, and Bi<sub>2</sub>S<sub>3</sub> exhibited the largest TRMC mobility-yield product (φμ<sub>TRMC</sub>) and longest lifetime. We also plotted on the same graph OPTP and TRMC transients for Bi<sub>2</sub>S<sub>3</sub> thin films, measured under similar excitation fluence (~70 μJ cm<sup>-2</sup>) as shown in Figure S8. Interestingly, the decays are self-consistent across the entire time scale, thus further validating our combined OPTP and TRMC approach. In addition, the ultralong lifetime observed from the Bi<sub>2</sub>S<sub>3</sub> thin films could be attributed to the shallow trap states and the resulting facile trapping-detrapping processes.<sup>26,30,31</sup> TRMC results (Table 1) also show that AgBiS<sub>2</sub> exhibits a considerably higher charge-carrier mobility compared with the antimony chalcogenides, thus confirming the OPTP finding on a longer time scale.

To quantify the charge-carrier dynamics in these materials, we performed fluence dependent OPTP and TRMC measurements. Owing to the possible presence of recombination mechanisms dependent on the charge-carrier density *n*,<sup>32</sup> fluence dependent measurements are needed to disentangle the different contributions. Crucially, to interpret these data sets, we used the well-established model expressed through the rate equation

$$\frac{dn}{dt} = -k_1 n - k_2 n^2 \quad (3)$$

where *k*<sub>1</sub> describes monomolecular recombination processes (e.g., exciton formation or trap assisted recombination) and *k*<sub>2</sub> represents the bimolecular recombination constant and reflects the electron–hole recombination. Based on fluence-dependent

OPTP measurements as shown in Figure S9, we are able to extract *k*<sub>1</sub> and *k*<sub>2</sub> of AgBiS<sub>2</sub> to be 1 × 10<sup>9</sup> s<sup>-1</sup> and 3 × 10<sup>-9</sup> cm<sup>3</sup> s<sup>-1</sup>, respectively. Similarly, Bi<sub>2</sub>S<sub>3</sub> presented a much lower *k*<sub>1</sub> of 1 × 10<sup>6</sup> s<sup>-1</sup> and a slightly larger *k*<sub>2</sub> of 7.5 × 10<sup>-9</sup> cm<sup>3</sup> s<sup>-1</sup>. Based on the obtained recombination constants and charge carrier mobility, we can determine the diffusion length of AgBiS<sub>2</sub> and Bi<sub>2</sub>S<sub>3</sub> to be 80 and 400 nm, respectively, which is comparable to the absorption depth (20 nm~100 nm) inferred from the high absorption coefficient (1 × 10<sup>5</sup>~5 × 10<sup>5</sup> cm<sup>-1</sup>). It also suggests that these bismuth-based chalcogenide thin films have a sufficient charge extraction ability for thin film optoelectronics.<sup>33</sup> We have also tried to conduct the same measurements for antimony-based chalcogenides. However, the OPTP decay of Sb<sub>2</sub>S<sub>3</sub> and AgSbS<sub>2</sub> was too fast to allow precise extraction of the recombination rate constants.

We also carried out fluence-dependent TRMC measurements, and compared the mobility values retrieved from the TRMC decays as shown in Figure 3a. Interestingly, both Sb<sub>2</sub>S<sub>3</sub> and AgSbS<sub>2</sub> showed increased mobility with the decrease of excitation intensity, as the recombination increased with the increase of light intensity. Such fluence-dependent charge-carrier dynamics is mainly attributed to the limited time-resolution of the TRMC measurements, which have also been observed from other solution-processed semiconductors, such as hybrid perovskites.<sup>31</sup> It is also worth noting that AgSbS<sub>2</sub> thin films did not show a strong enough signal at a low fluence, and we could not extract reliable mobility values. AgBiS<sub>2</sub> samples also exhibited similar fluence dependency. However, bismuth sulfide showed a distinct trend, that is, the mobility is almost independent of the pump fluence. Furthermore, Figure 3b,c

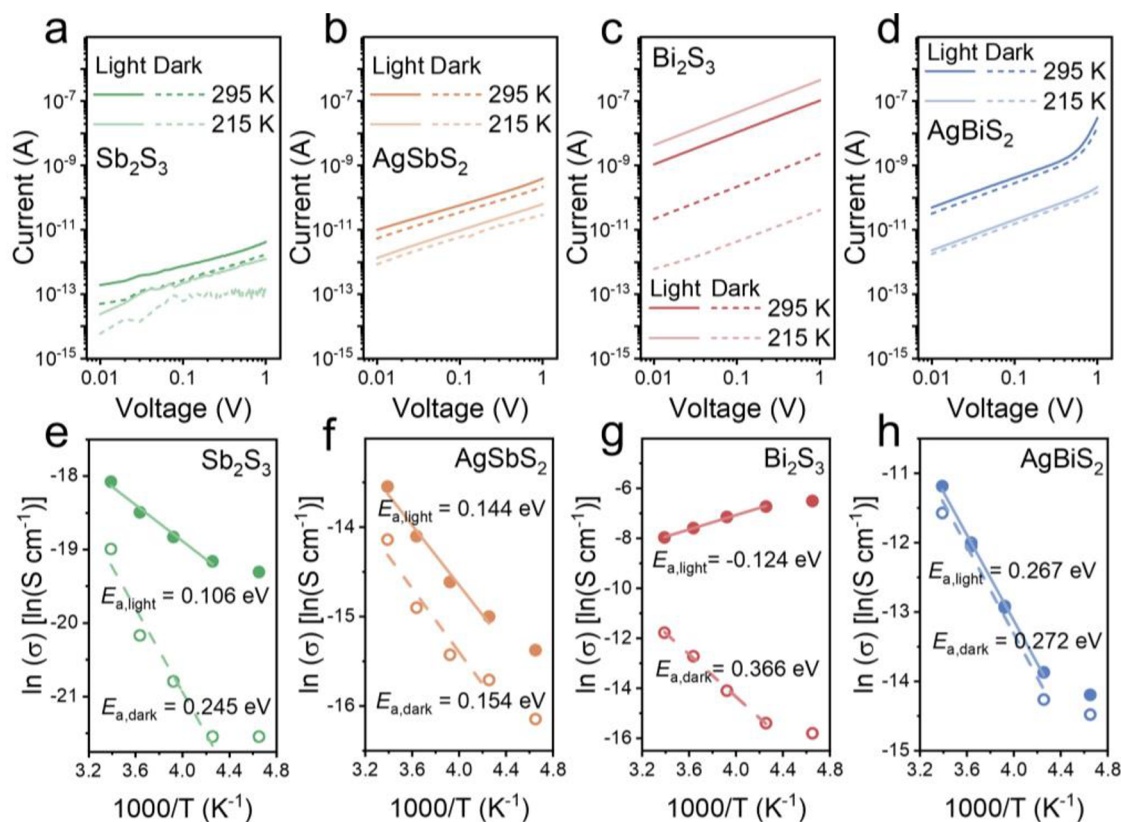


**Figure 4.** Comparison of the dark and photoconductivity of the solution-processed (a)  $\text{Sb}_2\text{S}_3$ , (b)  $\text{AgSbS}_2$ , (c)  $\text{Bi}_2\text{S}_3$ , and (d)  $\text{AgBiS}_2$  thin films, measured based on laser etched ITO electrodes with a channel width of  $100\ \mu\text{m}$ . The light intensity was set to be  $\sim 100\ \mu\text{W cm}^{-2}$ . Fitting of the temperature dependent dark current and photoconductivity, (e)  $\text{Sb}_2\text{S}_3$ , (f)  $\text{AgSbS}_2$ , (g)  $\text{Bi}_2\text{S}_3$ , and (h)  $\text{AgBiS}_2$ .

also compares the fluence-dependent OPTP traces of the  $\text{Bi}_2\text{S}_3$  and  $\text{AgBiS}_2$  samples, and we also observed the same trend that the  $\text{Bi}_2\text{S}_3$  thin films showed almost identical decays after 10 ps, but the  $\text{AgBiS}_2$  films showed typical fluence dependent OPTP decays. In the long time-scale, the  $\text{Bi}_2\text{S}_3$  thin films also showed fluence-independent TRMC dynamics (Figure 3d). Furthermore, by varying the excitation wavelength of the laser pulses, we can modulate the generation profiles within the samples. For example, chalcogenide thin films possess extremely high absorption coefficients for blue (450 nm) photons, thereby giving rise to a charge-carrier generation profile mainly located near the surface of samples facing the incident light. On the other hand, longer wavelength photons (e.g., near the bandgap) will experience lower absorption coefficients, thus resulting in a more homogeneous charge-carrier density profile across the sample. Normally, the TRMC dynamics should also be wavelength-dependent due to the difference on generation profiles.<sup>31,34,35</sup> However, the bismuth sulfide samples also showed wavelength-independent TRMC dynamics (Figure 3e), which could be attributed to the relatively high trap density and the trapping/detrapping processes of the shallow traps.<sup>36</sup> To rule out the influence of nanostructure on the charge carrier dynamics of  $\text{Bi}_2\text{S}_3$  thin films, we also prepared thin films based on precursors with various thiourea-bismuth (S-Bi) ratios. Interestingly, with the increase of the S-Bi ratio, the morphology changed dramatically, that is, the length of the nanorods increased but the diameter reduced, as shown in Figure S10a–c. However, the TRMC decays of these samples were almost identical (Figure S10d–f). Hence, we would safely conclude that the ultralong and fluence independent carrier-

dynamics is a key feature of the “bulk”  $\text{Bi}_2\text{S}_3$  and not significantly affected by the morphology.

Moreover, we also evaluated the dark current and photoconductivity of these chalcogenide thin films by laser etching of the indium tin oxide (ITO) electrodes with a channel width of  $100\ \mu\text{m}$ , as shown in Figure 4. The  $\text{Sb}_2\text{S}_3$  thin films showed extremely low dark current, reflecting the low conductivity of  $5.2 \times 10^{-9}\ \text{S cm}^{-1}$ , which is in line with the largest bandgap and lowest Urbach energy. On the contrary, the  $\text{AgSbS}_2$  films exhibited a remarkably increased dark current and conductivity of  $7.2 \times 10^{-7}\ \text{S cm}^{-1}$ . In addition, the  $\text{Sb}_2\text{S}_3$  and  $\text{AgSbS}_2$  samples showed a noticeable photoconductivity gain and slight temperature-dependence (Figures S11 and S12). These results are also consistent with the short carrier lifetime of antimony-based chalcogenide thin films according to the definition of photoconductivity gain ( $g$ ) given by

$$g = \frac{\tau}{t_{\text{tr}}} \quad (4)$$

$$t_{\text{tr}} = \frac{L^2}{V\mu} \quad (5)$$

where  $\tau$  is the carrier lifetime,  $t_{\text{tr}}$  is the carrier transient time,  $L$  is the charge transport length,  $\mu$  is the carrier mobility, and  $V$  is the bias voltage. Furthermore, we can also infer the charge-carrier density ( $n$ ) based on the measured charge-carrier mobility and conductivity ( $\sigma$ ), according to

$$n = \frac{\sigma}{q\mu} \quad (6)$$

where  $q$  is the elementary charge. Interestingly, we found the Ag-containing antimony-based samples exhibited increased carrier density of  $2.3 \times 10^{15} \text{ cm}^{-3}$ , compared with the  $\text{Sb}_2\text{S}_3$  films of  $1.1 \times 10^{13} \text{ cm}^{-3}$ . The lower charge-carrier density may create a wider depletion region in terms of PN junctions, which is beneficial for charge separation. That could be a reason why it has been possible to fabricate  $\text{Sb}_2\text{S}_3$ -based solar cells with relatively thick junctions and still achieve a relatively high PCE of >8%.<sup>12</sup> The bismuth-based films not only possess higher charge-carrier mobility but also high background charge-carrier density, and the resulting dark current and conductivity are extremely high, which may limit the performance of thin-film-based photodiodes. In addition, the  $\text{Bi}_2\text{S}_3$ -based chalcogenide thin films exhibited the largest on/off ratio between the light and dark current under the same illumination, indicating the largest photoconductive gain. It could be easily correlated with the longest lifetime, and will be beneficial for photoconductors (Figure S13). Intriguingly, we also found both the dark and light currents of the  $\text{Bi}_2\text{S}_3$  and  $\text{AgBiS}_2$  photoconductors are highly dependent on the temperature (Figures S14 and S15). We can also compare their activation energy ( $E_a$ ) from the temperature conductivity as shown in Figure 4e–h. Furthermore,  $\text{Bi}_2\text{S}_3$  samples showed increased photocurrent with decreasing temperature, which is unusual, compared with other chalcogenide thin films. The unusual temperature-dependent photoconductivity and light intensity-dependent TRMC decays of  $\text{Bi}_2\text{S}_3$  may be related to the relatively high trap density and large activation energy. It has been also suggested that the charge transport of  $\text{Bi}_2\text{S}_3$  thin films is significantly affected by the impurity and defects.<sup>8</sup> The decreased temperature could effectively reduce the charge recombination and enhance the charge transport.<sup>8</sup> Hence, how to reduce the charge trapping and recombination at room temperature could be an interesting topic for future study. The relatively small photoconductive gain of  $\text{AgBiS}_2$  also suggests that the active layer of  $\text{AgBiS}_2$ -based photodiodes should not be too thick due to the inferior charge-carrier lifetime.

In conclusion, we prepared antimony- and bismuth-based chalcogenide thin films via solution-processing techniques. Their crystallinity, morphology, and optical properties were systematically investigated and compared. We also studied the charge-carrier dynamics of these chalcogenide thin films with pump–probe techniques. As a result, we provide a complete characterization of the optoelectronic properties, such as charge-carrier mobility, lifetimes, and recombination rate constants. We also performed the temperature-dependent photoconductivity and revealed the influence of temperature on charge-carrier transport. To sum up, the main findings of this work are as follows: i) antimony-based chalcogenide thin films present lower mobilities compared with the bismuth-based samples; ii)  $\text{Bi}_2\text{S}_3$  samples showed distinct fluence and temperature-dependent optoelectronic properties, which are promising for photoconductors; iii)  $\text{Sb}_2\text{S}_3$  thin films have the lowest carrier density and sharpest absorption onset; iv)  $\text{AgBiS}_2$  possess the highest mobility but also high charge-carrier density, indicating that thin junctions are required for photodiodes. Overall, this work provides a fundamental analysis of the optoelectronic properties of recently developed solution-processed chalcogenide thin films, which provides a unified examination of the frontiers of chalcogenide materials and their suitability for application in specific optoelectronic devices.

## ■ ASSOCIATED CONTENT

### Supporting Information

The Supporting Information is available free of charge at <https://pubs.acs.org/doi/10.1021/acsenerylett.3c00140>.

Experimental details; supplementary notes of OPTP and TRMC; supplementary figures of optical photos, SEM images, transmittance and reflectance spectra; temperature dependent  $I$ – $V$  curves (PDF)

## ■ AUTHOR INFORMATION

### Corresponding Authors

**Laura M. Herz** — Department of Physics, University of Oxford, Oxford OX1 3PU, United Kingdom; Institute for Advanced Study, Technical University of Munich, 85748 Garching, Germany; [orcid.org/0000-0001-9621-334X](https://orcid.org/0000-0001-9621-334X); Email: [Laura.Herz@physics.ox.ac.uk](mailto:Laura.Herz@physics.ox.ac.uk)

**Qianqian Lin** — Key Lab of Artificial Micro- and Nano-Structures of Ministry of Education of China, School of Physics and Technology, Wuhan University, Wuhan, Hubei 430072, People's Republic of China; Hubei LuoJia Laboratory, Wuhan, Hubei 430072, People's Republic of China; [orcid.org/0000-0002-6144-1761](https://orcid.org/0000-0002-6144-1761); Email: [q.lin@whu.edu.cn](mailto:q.lin@whu.edu.cn)

### Authors

**Zhenglin Jia** — Key Lab of Artificial Micro- and Nano-Structures of Ministry of Education of China, School of Physics and Technology, Wuhan University, Wuhan, Hubei 430072, People's Republic of China; Hubei LuoJia Laboratory, Wuhan, Hubei 430072, People's Republic of China

**Marcello Righetto** — Department of Physics, University of Oxford, Oxford OX1 3PU, United Kingdom

**Yujie Yang** — Key Lab of Artificial Micro- and Nano-Structures of Ministry of Education of China, School of Physics and Technology, Wuhan University, Wuhan, Hubei 430072, People's Republic of China; Hubei LuoJia Laboratory, Wuhan, Hubei 430072, People's Republic of China

**Chelsea Q. Xia** — Department of Physics, University of Oxford, Oxford OX1 3PU, United Kingdom

**Yanyan Li** — Key Lab of Artificial Micro- and Nano-Structures of Ministry of Education of China, School of Physics and Technology, Wuhan University, Wuhan, Hubei 430072, People's Republic of China; Hubei LuoJia Laboratory, Wuhan, Hubei 430072, People's Republic of China

**Ruiming Li** — Key Lab of Artificial Micro- and Nano-Structures of Ministry of Education of China, School of Physics and Technology, Wuhan University, Wuhan, Hubei 430072, People's Republic of China; Hubei LuoJia Laboratory, Wuhan, Hubei 430072, People's Republic of China

**Yuwei Li** — Key Lab of Artificial Micro- and Nano-Structures of Ministry of Education of China, School of Physics and Technology, Wuhan University, Wuhan, Hubei 430072, People's Republic of China; Hubei LuoJia Laboratory, Wuhan, Hubei 430072, People's Republic of China

**Bin Yu** — Key Lab of Artificial Micro- and Nano-Structures of Ministry of Education of China, School of Physics and Technology, Wuhan University, Wuhan, Hubei 430072, People's Republic of China; Hubei LuoJia Laboratory, Wuhan, Hubei 430072, People's Republic of China



**Yong Liu** — Key Lab of Artificial Micro- and Nano-Structures of Ministry of Education of China, School of Physics and Technology, Wuhan University, Wuhan, Hubei 430072, People's Republic of China

**Huiming Huang** — Key Lab of Artificial Micro- and Nano-Structures of Ministry of Education of China, School of Physics and Technology, Wuhan University, Wuhan, Hubei 430072, People's Republic of China

**Michael B. Johnston** — Department of Physics, University of Oxford, Oxford OX1 3PU, United Kingdom; [orcid.org/0000-0002-0301-8033](https://orcid.org/0000-0002-0301-8033)

Complete contact information is available at:

<https://pubs.acs.org/10.1021/acsenenergylett.3c00140>

## Author Contributions

#Zhenglin Jia and Marcello Righetto contributed equally.

## Notes

The authors declare no competing financial interest.

## ACKNOWLEDGMENTS

This work was financially supported by the National Natural Science Foundation of China (Grant No. 61875154), Wuhan Science and Technology Bureau (Grant No. 2022010801010108), and the project supported by the open fund of Hubei LuoJia Laboratory (Grant No. 220100042). This work was supported by the Engineering and Physical Sciences Research Council (EPSRC) UK. We thank the Core Facility of Wuhan University for the access to analytical equipment. L.M.H. thanks TUM-IAS for a Hans Fischer Senior Fellowship and Award.

## REFERENCES

- (1) Mao, Y.; Hu, Y. H.; Hu, X. Y.; Yao, L. Q.; Li, H.; Lin, L. M.; Tang, P.; Li, H.; Chen, S.; Li, J. M.; et al. Molten salts assisted interfacial engineering for efficient and low-cost full-inorganic antimony sulfide solar cells. *Adv. Funct. Mater.* **2022**, *32*, 2208409.
- (2) Kondrotas, R.; Chen, C.; Tang, J. Sb<sub>2</sub>S<sub>3</sub> solar cells. *Joule* **2018**, *2* (5), 857–878.
- (3) Choi, Y. C.; Lee, D. U.; Noh, J. H.; Kim, E. K.; Seok, S. I. Highly improved Sb<sub>2</sub>S<sub>3</sub> sensitized-inorganic–organic heterojunction solar cells and quantification of traps by deep-level transient spectroscopy. *Adv. Funct. Mater.* **2014**, *24* (23), 3587–3592.
- (4) Rath, A. K.; Bernechea, M.; Martinez, L.; Konstantatos, G. Solution-Processed Heterojunction Solar Cells Based on p-type PbS Quantum Dots and n-type Bi<sub>2</sub>S<sub>3</sub> Nanocrystals. *Adv. Mater.* **2011**, *23* (32), 3712–3717.
- (5) Bera, A.; Das Mahapatra, A.; Mondal, S.; Basak, D. Sb<sub>2</sub>S<sub>3</sub>/Spiro-OMeTAD inorganic–organic hybrid p–n junction diode for high performance self-powered photodetector. *ACS Appl. Mater. Interfaces* **2016**, *8* (50), 34506–34512.
- (6) Konstantatos, G.; Levina, L.; Tang, J.; Sargent, E. H. Sensitive solution-processed Bi<sub>2</sub>S<sub>3</sub> nanocrystalline photodetectors. *Nano Lett.* **2008**, *8* (11), 4002–4006.
- (7) Yang, Y.; Huang, H.; Bai, S.; Yao, F.; Lin, Q. Optoelectronic modulation of silver antimony sulfide thin films for photodetection. *J. Phys. Chem. Lett.* **2022**, *13* (34), 8086–8090.
- (8) Kilcoyne, C.; Ali, A. H.; Alsaqqa, A. M.; Rahman, A. A.; Whittaker-Brooks, L.; Sambandamurthy, G. Gate-tunable transport characteristics of Bi<sub>2</sub>S<sub>3</sub> nanowire transistors. *Solid State Commun.* **2018**, *270*, 135–139.
- (9) Dashairya, L.; Sharma, S.; Rath, A.; Saha, P.; Basu, S. Solar-light-driven photocatalysis by Sb<sub>2</sub>S<sub>3</sub>/carbon based composites towards degradation of noxious organic pollutants. *Mater. Chem. Phys.* **2021**, *273*, 125120.
- (10) Zhang, Z.; Wang, W.; Wang, L.; Sun, S. Enhancement of visible-light photocatalysis by coupling with narrow-band-gap semiconductor: a case study on Bi<sub>2</sub>S<sub>3</sub>/Bi<sub>2</sub>WO<sub>6</sub>. *ACS Appl. Mater. Interfaces* **2012**, *4* (2), 593–597.
- (11) Tang, R.; Wang, X.; Jiang, C.; Li, S.; Jiang, G.; Yang, S.; Zhu, C.; Chen, T. Vacuum assisted solution processing for highly efficient Sb<sub>2</sub>S<sub>3</sub> solar cells. *J. Mater. Chem. A* **2018**, *6* (34), 16322–16327.
- (12) Wang, S.; Zhao, Y.; Che, B.; Li, C.; Chen, X.; Tang, R.; Gong, J.; Wang, X.; Chen, G.; Chen, T.; et al. A novel multi-sulfur source collaborative chemical bath deposition technology enables 8%-efficiency Sb<sub>2</sub>S<sub>3</sub> planar solar cells. *Adv. Mater.* **2022**, *34* (41), 2206242.
- (13) Tang, R.; Wang, X.; Lian, W.; Huang, J.; Wei, Q.; Huang, M.; Yin, Y.; Jiang, C.; Yang, S.; Xing, G.; et al. Hydrothermal deposition of antimony selenosulfide thin films enables solar cells with 10% efficiency. *Nat. Energy* **2020**, *5* (8), 587–595.
- (14) Bernechea, M.; Cates, N.; Xercavins, G.; So, D.; Stavrinadis, A.; Konstantatos, G. Solution-processed solar cells based on environmentally friendly AgBiS<sub>2</sub> nanocrystals. *Nat. Photonics* **2016**, *10* (8), 521–525.
- (15) Wang, Y.; Kavanagh, S. R.; Burgués-Ceballos, I.; Walsh, A.; Scanlon, D. O.; Konstantatos, G. Cation disorder engineering yields AgBiS<sub>2</sub> nanocrystals with enhanced optical absorption for efficient ultrathin solar cells. *Nat. Photonics* **2022**, *16* (3), 235–241.
- (16) Kim, C.; Kozakci, I.; Kim, J.; Lee, S. Y.; Lee, J. Y. Highly efficient (> 9%) lead-free AgBiS<sub>2</sub> colloidal nanocrystal/organic hybrid solar cells. *Adv. Energy Mater.* **2022**, *12*, 2200262.
- (17) Zhang, L.; Zhu, C.; Chen, T. Solution processed AgSbS<sub>2</sub> film for efficient planar heterojunction solar cells. *Appl. Phys. Lett.* **2021**, *119* (15), 151906.
- (18) Rath, A. K.; Bernechea, M.; Martinez, L.; de Arquer, F.; Osmond, J.; Konstantatos, G. Solution-processed inorganic bulk nano-heterojunctions and their application to solar cells. *Nat. Photonics* **2012**, *6* (8), 529–534.
- (19) Jiang, L.; Li, Y.; Peng, J.; Cui, L.; Li, R.; Xu, Y.; Li, W.; Li, Y.; Tian, X.; Lin, Q. Solution-processed AgBiS<sub>2</sub> photodetectors from molecular precursors. *J. Mater. Chem. C* **2020**, *8* (7), 2436–2441.
- (20) Zhao, K.; Yang, J.; Zhong, M.; Gao, Q.; Wang, Y.; Wang, X.; Shen, W.; Hu, C.; Wang, K.; Shen, G.; et al. Direct polarimetric image sensor and wide spectral response based on quasi-1D Sb<sub>2</sub>S<sub>3</sub> nanowire. *Adv. Funct. Mater.* **2021**, *31* (6), 2006601.
- (21) Xu, Y.; Li, R.; Bai, S.; Li, Y.; Jia, Z.; Yang, Y.; Cui, E.; Yao, F.; Wang, D.; Lei, C.; et al. Chalcogenide-based narrowband photodetectors for imaging and light communication. *Adv. Funct. Mater.* **2022**, 2212523.
- (22) Huang, H.; Yang, Y.; Chen, H.; Qin, F.; Yu, B.; Wang, R.; Cao, Q.; Wang, T.; Lin, Q. Interfacial engineering of high-performance, solution-processed Sb<sub>2</sub>S<sub>3</sub> phototransistors. *ACS Appl. Mater. Interfaces* **2022**, *14*, 57419.
- (23) Jiang, L.; Huang, H.; Gui, F.; Xu, Y.; Lin, Q. Ultrasensitive UV-NIR broadband phototransistors based on AgBiS<sub>2</sub>–organic hybrid films. *J. Mater. Chem. C* **2021**, *9* (24), 7583–7590.
- (24) Langford, J. I.; Wilson, A. Scherrer after sixty years: a survey and some new results in the determination of crystallite size. *J. Appl. Crystallogr.* **1978**, *11* (2), 102–113.
- (25) Adhyaksa, G. W.; Brittan, S.; Āboliņš, H.; Lof, A.; Li, X.; Keel, J. D.; Luo, Y.; Duevski, T.; Heeren, R. M.; Ellis, S. R.; et al. Understanding detrimental and beneficial grain boundary effects in halide perovskites. *Adv. Mater.* **2018**, *30* (52), 1804792.
- (26) Han, D.; Du, M.-H.; Dai, C.-M.; Sun, D.; Chen, S. Influence of defects and dopants on the photovoltaic performance of Bi<sub>2</sub>S<sub>3</sub>: first-principles insights. *J. Mater. Chem. A* **2017**, *5* (13), 6200–6210.
- (27) Li, X.; Wu, Y.; Zhang, S.; Cai, B.; Gu, Y.; Song, J.; Zeng, H. CsPbX<sub>3</sub> quantum dots for lighting and displays: room-temperature synthesis, photoluminescence superiorities, underlying origins and white light-emitting diodes. *Adv. Funct. Mater.* **2016**, *26* (15), 2435–2445.
- (28) Luo, L.; Men, L.; Liu, Z.; Mudryk, Y.; Zhao, X.; Yao, Y.; Park, J. M.; Shinar, R.; Shinar, J.; Ho, K.-M.; et al. Ultrafast terahertz

snapshots of excitonic Rydberg states and electronic coherence in an organometal halide perovskite. *Nat. Commun.* **2017**, *8* (1), 1–8.

(29) Lian, W.; Jiang, C.; Yin, Y.; Tang, R.; Li, G.; Zhang, L.; Che, B.; Chen, T. Revealing composition and structure dependent deep-level defect in antimony trisulfide photovoltaics. *Nat. Commun.* **2021**, *12* (1), 1–7.

(30) Guo, D.; Andaji Garmaroudi, Z.; Abdi-Jalebi, M.; Stranks, S. D.; Savenije, T. J. Reversible removal of intermixed shallow states by light soaking in multication mixed halide perovskite films. *ACS Energy Lett.* **2019**, *4* (10), 2360–2367.

(31) Guse, J. A.; Soufiani, A. M.; Jiang, L.; Kim, J.; Cheng, Y.-B.; Schmidt, T. W.; Ho-Baillie, A.; McCamey, D. R. Spectral dependence of direct and trap-mediated recombination processes in lead halide perovskites using time resolved microwave conductivity. *Phys. Chem. Chem. Phys.* **2016**, *18* (17), 12043–12049.

(32) Chanana, A.; Liu, X.; Zhang, C.; Vardeny, Z. V.; Nahata, A. Ultrafast frequency-agile terahertz devices using methylammonium lead halide perovskites. *Sci. Adv.* **2018**, *4* (5), eaar7353.

(33) Kaienburg, P.; Krückemeier, L.; Lübke, D.; Nelson, J.; Rau, U.; Kirchartz, T. How solar cell efficiency is governed by the  $\alpha\mu\tau$  product. *Phys. Rev. Res.* **2020**, *2* (2), 023109.

(34) Bi, Y.; Hutter, E. M.; Fang, Y.; Dong, Q.; Huang, J.; Savenije, T. J. Charge carrier lifetimes exceeding 15  $\mu$ s in methylammonium lead iodide single crystals. *J. Phys. Chem. Lett.* **2016**, *7* (5), 923–928.

(35) Wu, W.; Zhou, Y.; Wang, J.; Shao, Y.; Kong, D.; Gao, Y.; Wang, Y. The pump fluence and wavelength-dependent ultrafast carrier dynamics and optical nonlinear absorption in black phosphorus nanosheets. *Nanophotonics* **2020**, *9* (7), 2033–2043.

(36) Li, Y.; Jia, Z.; Yang, Y.; Yao, F.; Liu, Y.; Lin, Q. Shallow traps-induced ultra-long lifetime of metal halide perovskites probed with light-biased time-resolved microwave conductivity. *Appl. Phys. Rev.* **2023**, *10* (1), 011406.

## Recommended by ACS

### Oxygen Management to Avoid Photo-Inactive Cd(S,Se) for Efficient Cd(Se,Te) Solar Cells

Deng-Bing Li, Yanfa Yan, *et al.*

FEBRUARY 20, 2023  
ACS ENERGY LETTERS

READ 

### Dual Optimization of Bulk and Interface via the Synergistic Effect of Ligand Anchoring and Hole Transport Dopant Enables 23.28% Efficiency Inverted Perovskite Solar Cells

Xianyong Zhou, Baomin Xu, *et al.*

FEBRUARY 13, 2023  
ACS NANO

READ 

### Bi<sub>2</sub>S<sub>3</sub> Electron Transport Layer Incorporation for High-Performance Heterostructure HgTe Colloidal Quantum Dot Infrared Photodetectors

Ji Yang, Jiang Tang, *et al.*

JANUARY 09, 2023  
ACS PHOTONICS

READ 

### Bifacial Thermophotovoltaic Energy Conversion

A. Datas.

FEBRUARY 09, 2023  
ACS PHOTONICS

READ 

Get More Suggestions >